Universal Quantum Viscosity in a Unitary Fermi Gas

C. Cao, *et al.*

Science **331**, 58 (2011);
DOI: 10.1126/science.1195219

This copy is for your personal, non-commercial use only.

If you wish to distribute this article to others, you can order high-quality copies for your colleagues, clients, or customers by clicking here.

Permission to republish or repurpose articles or portions of articles can be obtained by following the guidelines here.

The following resources related to this article are available online at www.sciencemag.org (this infomation is current as of October 18, 2011):

Updated information and services, including high-resolution figures, can be found in the online version of this article at:
http://www.sciencemag.org/content/331/6013/58.full.html

Supporting Online Material can be found at:
http://www.sciencemag.org/content/suppl/2010/12/06/science.1195219.DC1.html

This article **cites 22 articles**, 3 of which can be accessed free:
http://www.sciencemag.org/content/331/6013/58.full.html#ref-list-1

Downloaded from www.sciencemag.org on October 18, 2011

Science (print ISSN 0036-8075; online ISSN 1095-9203) is published weekly, except the last week in December, by the American Association for the Advancement of Science, 1200 New York Avenue NW, Washington, DC 20005. Copyright 2011 by the American Association for the Advancement of Science; all rights reserved. The title *Science* is a registered trademark of AAAS.

to the formation of spicular features in He II 304 Å (~0.1 MK). These TR spicules appear with a time delay of around 10 to 20 s, reach much larger heights (~10 to 20 Mm), and typically fall back to the surface within a matter of several minutes, following a parabolic path (Fig. 3 and fig. S5). Despite the enormous line-of-sight superposition at the limb, we often also observe a coronal counterpart of chromospheric/TR spicules (Fig. 3 and fig. S5) in the Fe IX 171 Å images. At the bottom, this takes the form of a dark feature that corresponds to the bright Ca II H feature (movie S8), likely from continuum absorption from neutral hydrogen and helium (*21*). During the later stages, the dark feature disappears (likely because heating reduces the amount of neutral hydrogen and helium), and bright coronal counterparts propagate upward into the coronal hole with similar velocities as the apparent motions of the chromospheric spicules (fig. S5). These coronal counterparts appear to be related to the propagating disturbances in coronal holes that have previously been interpreted as waves (*22*) and more recently linked to upflows (*23*, *24*).

Our observations support a scenario in which chromospheric plasma is propelled upward with speeds of ~50 to 100 km/s, with the bulk of the mass rapidly heated to TR temperatures (~0.02 to 0.1 MK), after which it returns to the surface (invisible to chromospheric passbands). Directly associated with these jets, plasma is heated to coronal temperatures of at least 1 to 2 MK, at the bottom during the initial stages, and both along and toward the top of the chromospheric feature later on. The coronal counterparts of the jets are seen to rapidly propagate upward, likely as a result of strong upflows and/or thermal conduction or waves. Based on the ubiquity of these events and the observed coronal intensities, we estimate that these events carry a mass flux density of 1.5×10^{-9} g/cm^2/s and an energy flux density of $\sim 2 \times 10^6$ erg/cm^2/s into the corona (*25*). This is of the order that is required to sustain the energy lost from the active-region corona (*26*). Given the conservative nature of our estimate, these events are likely to play a substantial role in the coronal energy balance.

Although early models have implicated the heating of chromospheric spicules in the coronal heating problem (*6*), the detailed thermal and spatiotemporal evolution we observed is not compatible with any of the well-established models for coronal heating: None of those predict such strong upflows (driven from below) at chromospheric temperatures (*2*, *27*). These models typically assume energy deposition in the corona, which leads to heating and evaporation of plasma from the chromospheric mass reservoir, driven by thermal conduction from above. Recent advanced numerical models do predict heating rates per particle that reach their maximum in the upper chromosphere (*28*, *29*), which is compatible with our observations. Some analytical models also suggest that dissipation of current sheets resulting from the shuffling of ubiquitous mixed-polarity fields on small scales can provide coronal heating at low heights (*30*). However, there are currently no models for what drives and heats the observed jets (*31*). These first detailed observations of individual coronal heating events highlight the importance of the chromosphere and magnetohydrodynamic/plasma physics approaches for a better understanding of heating in the solar atmosphere.

References and Notes

1. B. Edlen, *Z. Astrophysik* **22**, 30 (1942).
2. J. A. Klimchuk, *Sol. Phys.* **234**, 41 (2006).
3. E. N. Parker, *Geophys. Astrophys. Fluid Dyn.* **50**, 229 (1990).
4. C. J. Schrijver, A. W. Sandman, M. J. Aschwanden, M. L. DeRosa, *Astrophys. J.* **615**, 512 (2004).
5. M. J. Aschwanden, R. Nightingale, P. Boerner, *Astrophys. J.* **656**, 577 (2007).
6. G. W. Pneuman, R. A. Kopp, *Sol. Phys.* **57**, 49 (1978).
7. R. G. Athay, T. E. Holzer, *Astrophys. J.* **255**, 743 (1982).
8. G. L. Withbroe, *Astrophys. J.* **267**, 825 (1983).
9. K. P. Dere, J.-D. F. Bartoe, G. E. Brueckner, *Sol. Phys.* **123**, 41 (1989).
10. R. Rutten, *ASP Conf. Ser.* **354**, 276 (2006)
11. B. De Pontieu *et al.*, *Pub. Astron. Soc. Jpn.* **59**, 655 (2007).
12. B. De Pontieu, S. W. McIntosh, V. H. Hansteen, C. J. Schrijver, *Astrophys. J.* **701**, L1 (2009).
13. J. Mariska, *Solar Transition Region* (Cambridge Astrophysics Series, vol. 23, Cambridge Univ. Press, New York, 1992).
14. Ø. Langangen *et al.*, *Astrophys. J.* **679**, L167 (2008).
15. L. Rouppe van der Voort, J. Leenaarts, B. de Pontieu, M. Carlsson, G. Vissers, *Astrophys. J.* **705**, 272 (2009).
16. T. Kosugi *et al.*, *Sol. Phys.* **243**, 3 (2007).
17. S. Tsuneta *et al.*, *Sol. Phys.* **249**, 167 (2008).
18. See materials and methods in the supporting online material (SOM) on *Science* Online.
19. J. L. Culhane *et al.*, *Sol. Phys.* **243**, 19 (2007).
20. H. Hara *et al.*, *Astrophys. J.* **678**, L67 (2008).
21. U. Anzer, P. Heinzel, *Astrophys. J.* **622**, 714 (2005).
22. D. Banerjee *et al.*, *Astron. Astrophys.* **499**, 29 (2009).
23. S. W. McIntosh, B. De Pontieu, *Astrophys. J.* **707**, 524 (2009).
24. S.W. McIntosh *et al.*, *Astron. Astrophys.* **510**, 2 (2010).
25. See SOM discussion.
26. E. R. Priest, *Solar Magnetohydrodynamics* (D. Reidel Publishing, Dordrecht, Netherlands, 1982).
27. S. Patsourakos, J. A. Klimchuk, *Astrophys. J.* **647**, 1452 (2006).
28. B. V. Gudiksen, A. Nordlund, *Astrophys. J.* **618**, 1031 (2005).
29. V. H. Hansteen, H. Hara, B. De Pontieu, M. Carlsson, *Astrophys. J.* **718**, 1070 (2010).
30. E. Priest, J. Heyvaerts, A. Title, *Astrophys. J.* **576**, 533 (2002).
31. A. Sterling, *Sol. Phys.* **196**, 79 (2000).
32. This work is supported by NASA grants NNX08AL22G and NNX08BA99G (to B.D.P. and S.W.M.), NASA contracts NNM07AA01C (Hinode) and NNG04EA00C (AIA), and the Research Council of Norway (M.C. and V.H.H.). The National Center for Atmospheric Research is sponsored by NSF. Hinode is a Japanese mission developed by the Institute of Space and Astronautical Science/Japan Aerospace Exploration Agency, with the National Astronomical Observatory of Japan as domestic partner and NASA and Science and Technology Facilities Council (UK) as international partners. It is operated in cooperation with the European Space Agency and the Norwegian Space Centre (Norway).

Supporting Online Material

www.sciencemag.org/cgi/content/full/331/6013/55/DC1
Materials and Methods
SOM Text
Figs. S1 to S5
References
Movies S1 to S9

13 September 2010; accepted 2 December 2010
10.1126/science.1197738

Universal Quantum Viscosity in a Unitary Fermi Gas

C. Cao,[1] E. Elliott,[1] J. Joseph,[1] H. Wu,[1] J. Petricka,[2] T. Schäfer,[3] J. E. Thomas[1]*

A Fermi gas of atoms with resonant interactions is predicted to obey universal hydrodynamics, in which the shear viscosity and other transport coefficients are universal functions of the density and temperature. At low temperatures, the viscosity has a universal quantum scale $\hbar\, n$, where n is the density and $\hbar$ is Planck's constant h divided by 2π, whereas at high temperatures the natural scale is $p_T^3/\hbar^2$, where p_T is the thermal momentum. We used breathing mode damping to measure the shear viscosity at low temperature. At high temperature T, we used anisotropic expansion of the cloud to find the viscosity, which exhibits precise $T^{3/2}$ scaling. In both experiments, universal hydrodynamic equations including friction and heating were used to extract the viscosity. We estimate the ratio of the shear viscosity to the entropy density and compare it with that of a perfect fluid.

Ultracold, strongly interacting Fermi gases are of broad interest because they provide a tunable tabletop paradigm for strongly interacting systems, ranging from high-temperature superconductors to nuclear matter. First observed in 2002, quantum degenerate, strongly interacting Fermi gases are being widely studied (*1*–*4*). To obtain strong interactions (characterized by a divergent s-wave scattering length), a bias magnetic field is used to tune the gas to a broad collisional (Feshbach) resonance, for which the range of the collision potential is small compared with the interparticle spacing. In this so-called unitary regime, the properties of the gas are universal functions of the density n and temperature T. The universal behavior of the equilibrium thermodynamic properties has been studied in detail (*5*–*11*), whereas the measurement of universal transport coefficients presents new challenges.

---

[1] Department of Physics, Duke University, Durham, NC 27708, USA. [2] Department of Physics, Gustavus Adolphus College, Saint Peter, MN 56082, USA. [3] Department of Physics, North Carolina State University, Raleigh, NC 27695, USA.

*To whom correspondence should be addressed. E-mail: jet@phy.duke.edu

The measurement of the viscosity is of particular interest in the context of a recent conjecture, derived using string theory methods, that defines a perfect normal fluid (*12*). An example of a nearly perfect fluid is the quark-gluon plasma produced in gold ion collisions, which exhibits almost perfect frictionless flow and is thought to be a good approximation to the state of matter that existed microseconds after the Big Bang (*13*). The conjecture states that the ratio of the shear viscosity η to the entropy density s has a universal minimum, $\eta/s \geq \hbar/(4\pi k_B)$, where $\hbar$ is Planck's constant h divided by 2π and k_B is the Boltzmann constant. This ratio is experimentally accessible in a trapped unitary Fermi gas, in which the entropy has been measured both globally (*6*, *9*) and locally (*10*, *11*) and the viscosity can be determined from hydrodynamic experiments (*14*–*17*), so that the predicted minimum ratio can be directly compared with that from Fermi gas experiments (*16*, *17*).

In a Fermi gas, the η/s ratio for the normal fluid is expected to reach a minimum just above the superfluid transition temperature (*16*). This can be understood by using dimensional analysis. Shear viscosity has units of momentum per area. For a unitary gas, the natural momentum is the relative momentum $\hbar\,k$ of a colliding pair of particles, whereas the natural area is the resonant s-wave collision cross section, $4\pi/k^2$ (*18*). Thus, $\eta \propto \hbar\,k^3$. At temperatures well below the Fermi temperature at which degeneracy occurs, the Fermi momentum sets the scale so that $k \simeq 1/L$, where L is the interparticle spacing. Then, $\eta \propto \hbar\,/L^3$, and $\eta \propto \hbar\,n$. For a normal fluid above the critical temperature, the scale of entropy density $s \simeq n\,k_B$, so that $\eta/s \simeq \hbar\,/k_B$. For much higher temperatures above the Fermi temperature, one expects that $\hbar\,k$ is comparable with the thermal momentum $p_T = \sqrt{2mk_BT}$, giving the scale $\eta \propto p_T^{\,3}/\hbar^2 \propto T^{3/2}/\hbar^2$.

To properly measure the shear viscosity with high precision over a wide temperature range, we used universal hydrodynamic equations, which contain both the friction force and the heating rate, to extract the viscosity from two experiments, one for each of two temperature ranges. For measurement at high temperatures, we observed the expansion dynamics of a unitary Fermi gas after release from a deep optical trap and demonstrated the predicted universal $T^{3/2}$ temperature scaling. For measurement at low temperatures, we used the damping rate of the radial breathing mode, using the raw cloud profiles from our previous work (*19*). The smooth joining of the data from the two measurement methods when heating is included (*20*), and the discontinuity of the data when heating is excluded, demonstrates the importance of including the heating as well as the friction force in the universal hydrodynamic analysis.

The experiments employ a 50-50 mixture of the two lowest hyperfine states of ^{6}Li, which was magnetically tuned to a broad Feshbach resonance and cooled by means of evaporation in the optical trap. The initial energy per particle E is measured from the trapped cloud profile (*20*).

In the high-temperature regime, the total energy of the gas E is larger than $2E_F$, well above the critical energy $E_c < 0.8E_F$ for the superfluid transition (*9*–*11*). In this case, the density profile is well fit by a Gaussian, $n(x,y,z,t) = n_0(t) \exp(-x^2/\sigma_x^{\,2}-y^2/\sigma_y^{\,2}-z^2/\sigma_z^{\,2})$, where $\sigma_i(t)$ is a time-dependent width, $n_0(t)=N/(\pi^{3/2}\sigma_x\sigma_y\sigma_z)$ is the central density, and N is the total number of atoms.

The aspect ratio $\sigma_x(t)/\sigma_z(t)$ was measured as a function of time after release so as to characterize the hydrodynamics, for different energies E between $2.3E_F$ and $4.6E_F$ (Fig. 1). We also took expansion data at one low-energy point $E = 0.6E_F$, where the viscosity is small as compared with that obtained at higher temperatures and the density profile is approximately a zero-temperature Thomas-Fermi distribution. The black curve in Fig. 1 shows the fit for zero viscosity and no free parameters. To obtain a high signal-to-background ratio, we measured the aspect ratio only up to 1.4. For comparison, the green dashed curve in Fig. 1 shows the prediction for a ballistic gas.

We determined the shear viscosity η by using a hydrodynamic description of the velocity field $\mathbf{v}(\mathbf{x},t)$ in terms of the scalar pressure and the shear viscosity pressure tensor,

$$m(\partial_t + \mathbf{v}\cdot\nabla)v_i = f_i + \sum_j \frac{\partial_j(\eta\,\sigma_{ij})}{n} \qquad (1)$$

where $\mathbf{f} = -\nabla P/n$ is the force per particle arising from the scalar pressure P and m is the atom mass. For a unitary gas, the bulk viscosity is predicted to vanish in the normal fluid (*21*, *22*), so we did not include it in the analysis for the expansion. The second term on the right describes the friction forces arising from the shear viscos-

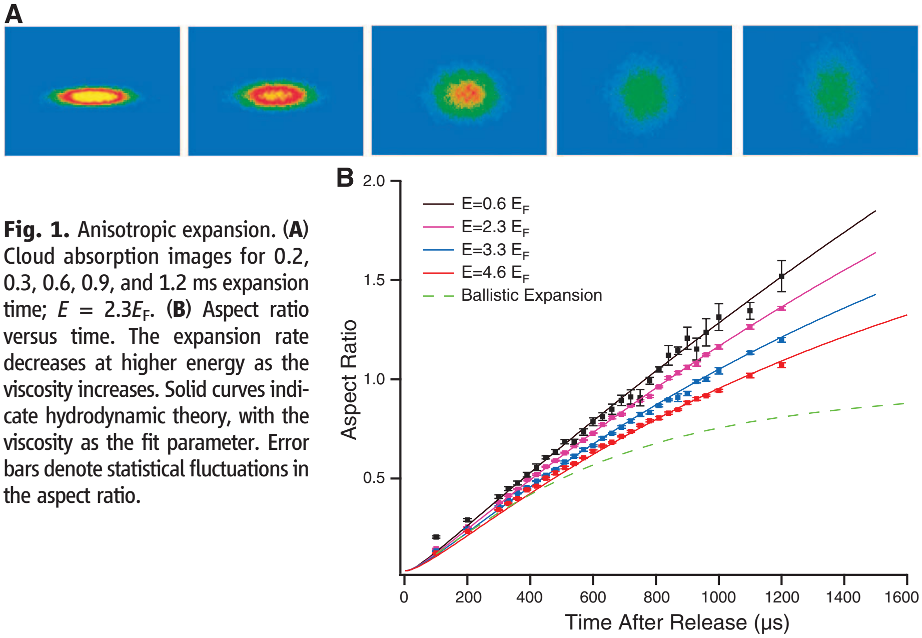

Fig. 1. Anisotropic expansion. (**A**) Cloud absorption images for 0.2, 0.3, 0.6, 0.9, and 1.2 ms expansion time; $E = 2.3E_F$. (**B**) Aspect ratio versus time. The expansion rate decreases at higher energy as the viscosity increases. Solid curves indicate hydrodynamic theory, with the viscosity as the fit parameter. Error bars denote statistical fluctuations in the aspect ratio.

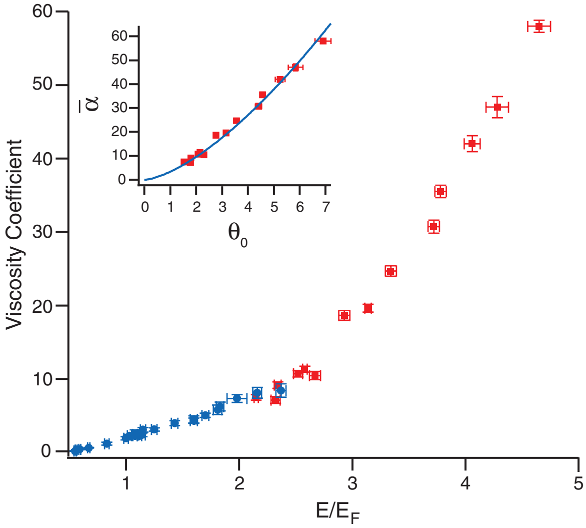

Fig. 2. Trap-averaged viscosity coefficient $\bar{\alpha} = \int d^3\mathbf{x}\,\eta/(\hbar N)$ versus initial energy per atom. Blue circles indicate breathing-mode measurements; red squares indicate anisotropic expansion measurements. Bars denote statistical error arising from the uncertainty in E and the cloud dimensions. (**Inset**) $\bar{\alpha}$ versus reduced temperature θ_0 at the trap center before release of the cloud. The blue curve shows the fit $\alpha_0 = \alpha_{3/2}\,\theta_0^{\,3/2}$, demonstrating the predicted universal high-temperature scaling. Bars denote statistical error arising from the uncertainty in θ_0 and $\bar{\alpha}$. A 3% systematic uncertainty in E_F and 7% in θ_0 arises from the systematic uncertainty in the absolute atom number (*20*).

ity, where $\sigma_{ij} = \partial v_i/\partial x_j + \partial v_j/\partial x_i - 2\delta_{ij}\nabla \cdot \mathbf{v}/3$ is symmetric and traceless.

For a unitary gas, the evolution equation for the pressure takes a simple form because $P = 2\mathcal{E}/3$ (*23*, *24*), where $\mathcal{E}$ is the local energy density (sum of the kinetic and interaction energy). Then, energy conservation and Eq. 1 implies $(\partial_t + \mathbf{v} \cdot \nabla + 5\nabla \cdot \mathbf{v}/3)P = 2 \cdot \dot{q}/3$. Here, the heating rate per unit volume times $\dot{q} = \eta\sigma_{ij}^2/2$ arises from friction from the relative motion of neighboring volume elements. To express this in terms of the force per particle (f_i), we differentiated this equation for P with respect to x_i and used the continuity equation for the density to obtain

$$\left(\partial_t + \mathbf{v} \cdot \nabla + \frac{2}{3}\nabla \cdot \mathbf{v}\right)f_{\mathrm{i}} + \sum_{\mathrm{j}} (\partial_{\mathrm{i}}v_{\mathrm{j}})f_{\mathrm{j}} - \frac{5}{3}(\partial_{\mathrm{i}}\nabla\cdot\mathbf{v})\frac{P}{n} = -\frac{2}{3}\frac{\partial_{\mathrm{i}}\dot{q}}{n} \qquad (2)$$

Force balance in the trapping potential $U_{\mathrm{trap}}(\mathbf{x})$, just before release of the cloud, determines the initial condition $f_{\mathrm{i}}(0) = \partial_{\mathrm{i}}U_{\mathrm{trap}}(\mathbf{x})$.

These hydrodynamic equations include both the force and the heating arising from viscosity. The solution is greatly simplified when the cloud is released from a deep, nearly harmonic trapping potential U_{trap} because $f_{\mathrm{i}}(0)$ is then linear in the spatial coordinate. If we neglect viscosity, the force per particle and hence the velocity field remain linear functions of the spatial coordinates as the cloud expands. Thus, $\partial_{\mathrm{i}}(\nabla \cdot \mathbf{v}) = 0$, and the pressure P does not appear in Eq. 2. Through numerical integration (*25*), we found that nonlinearities in the velocity field are very small, even if the viscosity is not zero, because dissipative forces tend to restore a linear flow profile. Hence, the evolution Eqs. 1 and 2 are only weakly dependent on the precise initial spatial profile of P and independent of the detailed thermodynamic properties.

We therefore assumed that the velocity field is exactly linear in the spatial coordinates. We took $f_{\mathrm{i}} = a_{\mathrm{i}}(t)x_{\mathrm{i}}$ and $\sigma_{\mathrm{i}}(t) = b_{\mathrm{i}}(t)\sigma_{\mathrm{i}}(0)$; the density changes by a scale transformation (*26*), where current conservation then requires $v_{\mathrm{i}} = x_{\mathrm{i}}\dot{b}_{\mathrm{i}}(t)/b_{\mathrm{i}}(t)$.

In general, the viscosity takes the universal form $\eta = \alpha(\theta)\hbar n$, where θ is the local reduced temperature and $\eta \rightarrow 0$ in the low-density region of the cloud (*20*, *27*). Using the measured trap frequencies, and Eqs. 1 and 2, the aspect ratio data are fit to determine the trap-averaged viscosity parameter, $\bar{\alpha} = (1/N\hbar)\int d^3\mathbf{x}\ \eta(\mathbf{x},t)$, which arises naturally independent of the spatial profile of and is equivalent to assuming η. Because θ has a zero convective derivative everywhere (in the zeroth-order adiabatic approximation) and the number of atoms in a volume element is conserved along a stream tube, $\bar{\alpha}$ is a constant that can be compared with predictions for the trapped cloud before release.

As shown in Fig. 1, the expansion data are very well fit over the range of energies studied, using $\bar{\alpha}$ as the only free parameter. We found that the friction force produces a curvature that matches the aspect ratio–versus-time data, whereas the indirect effect of heating is important in increasing the outward force, which increases the fitted $\bar{\alpha}$ by a factor of ≅2, as compared with that obtained when heating is omitted (*20*).

For measurements at low temperatures, where the viscosity is small, we determined $\bar{\alpha}$ from the damping rate of the radial breathing mode (*19*). For the breathing mode, the cloud radii change by a scale transformation of the form $b_{\mathrm{i}} = 1 + \epsilon_{\mathrm{i}}$, with $\epsilon_{\mathrm{i}} << 1$, and the heating rate in Eq. 2 is $\propto \dot{\epsilon}_{\mathrm{i}}^2$, which is negligible. Hence, the force per particle evolves adiabatically. Adding the trapping force to Eq. 1, one obtains the damping rate $1/\tau = \hbar\,\bar{\alpha}/(3m\langle x^2\rangle)$ (*20*, *28*).

The fitted viscosity coefficients $\bar{\alpha}$ for the entire energy range are shown in Fig. 2, which can be used to test predictions (*29*–*31*). Despite the large values of $\bar{\alpha}$ at the higher energies, the viscosity causes only a moderate perturbation to the adiabatic expansion, as shown by the expansion data and the fits in Fig. 1. The breathing mode data and expansion data smoothly join, provided that the heating rate is included in the analysis. In contrast, omitting the heating rate produces a discontinuity between the high- and low-temperature viscosity data (*20*). The agreement between these very different measurements when heating is included shows that hydrodynamics in the universal regime is well described by Eqs. 1 and 2.

To test the prediction of the $T^{3/2}$ temperature scaling in the high-temperature regime, we assumed that η relaxes to the equilibrium value in the center of the trap but vanishes in the low-density region so that $\bar{\alpha}$ is well defined. This behavior is predicted by kinetic theory (*27*). We expect that $\bar{\alpha} \cong \alpha_0$, where $\eta_0 = \alpha_0\ \hbar\ n_0$ is the viscosity at the trap center before release. At high temperatures (*15*),

$$\alpha_0 = \alpha_{3/2}\ \theta_0^{3/2} \qquad (3)$$

where $\alpha_{3/2}$ is a universal coefficient. Because θ has a zero convective derivative everywhere (in the zeroth-order adiabatic approximation), θ_0 at the trap center has a zero time derivative, and α_0 is therefore constant, as is $\bar{\alpha}$.

The inset in Fig. 2 shows the high-temperature (expansion) data for $\bar{\alpha}$ versus the initial reduced temperature at the trap center, θ_0. Here, $\theta_0 = T_0/T_{\mathrm{F}}(n_0) = (T_0/T_{\mathrm{FI}})(n_{\mathrm{I}}/n_0)^{2/3}$. The local Fermi temperature $T_{\mathrm{F}}(n_0) = \hbar^2(3\pi^2 n_0)^{2/3}/(2mk_{\mathrm{B}})$, and $T_{\mathrm{FI}} = E_{\mathrm{F}}\ /k_{\mathrm{B}} = T_{\mathrm{F}}\ (n_{\mathrm{I}})$ is the ideal gas Fermi temperature at the trap center. n_{I} is the ideal gas central density for a zero-temperature Thomas-Fermi distribution. We used $(n_{\mathrm{I}}/n_0)^{2/3} = 4(\sigma^2{}_z/\sigma^2{}_{\mathrm{Fz}})/\pi^{1/3}$ and obtained the initial T_0/T_{FI} from the cloud profile (*20*).

The excellent fit of Eq. 3 to the data (Fig. 2, inset) demonstrates that at high temperature, the viscosity coefficient very well obeys the $\theta_0^{3/2}$ scaling, which is in agreement with predictions (*15*). Eq. 3 predicts that α_0 scales nearly as E^3 because $\theta_0 \propto T_0/n_0^{2/3} \propto E^2$. This explains the factor of ≅10 increase in the viscosity coefficients as the initial energy is increased from $E = 2.3E_{\mathrm{F}}$ to $E = 4.6E_{\mathrm{F}}$.

A precise comparison between the viscosity data and theory requires calculation of the trap-average $\bar{\alpha}$ from the local shear viscosity, where the relation is tightly constrained by the observed $T^{3/2}$ scaling. Our simple approximation $\bar{\alpha} \cong \alpha_0$ yields $\alpha_{3/2} = 3.4(0.03)$, where 0.03 is the statistical error from the fit. A better estimate based on a relaxation model (*29*) shows that $\bar{\alpha} = 1.3\ \alpha_0$ at high T, yielding $\alpha_{3/2} = 2.6$. At sufficiently high temperature, the mean free path becomes longer than the interparticle spacing because the unitary collision cross section decreases with increasing energy. In this limit, a two-body Boltzmann equation description of the viscosity is valid. For a Fermi gas in a 50-50 mixture of two spin states, a variational calculation (*15*) yields $\alpha_{3/2} = 45\pi^{3/2}/(64\sqrt{2}) = 2.77$, which is in reasonable agreement with the fitted values.

Lastly, Fig. 3 shows an estimate of the ratio of $\eta/s = \alpha\hbar n/s = (\hbar/k_{\mathrm{B}})\alpha/(s/nk_{\mathrm{B}}) \cong (\hbar/k_{\mathrm{B}})\,\bar{\alpha}/S$, where S is the average entropy per particle of the trapped gas in units of k_{B}. We obtain S in the low-

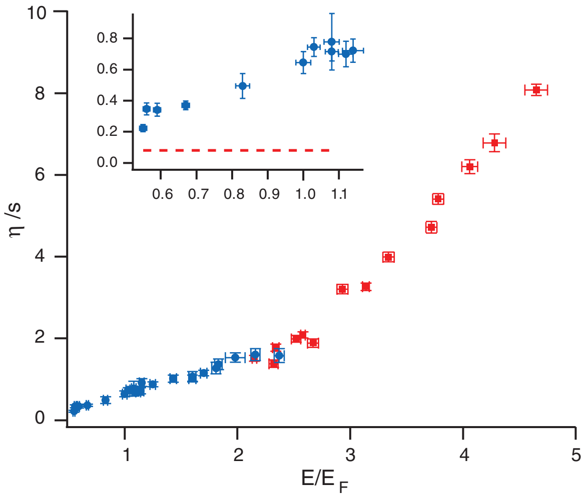

Fig. 3. Estimated ratio of the shear viscosity to the entropy density. Blue circles indicate breathing-mode measurements; red squares indicate anisotropic expansion measurements. (**Inset**) The red dashed line denotes the string theory limit. Bars denote statistical error arising from the uncertainty in E, $\bar{\alpha}$, and S (*20*).

temperature regime from (*9*), which joins smoothly to the second virial coefficient approximation for S in the high-temperature regime (*20*). The Fig. 3 inset shows the low-temperature behavior, which is about five times the string theory limit (Fig. 3, inset, red dashed line) near the critical energy E_c/E_F = 0.7–0.8 (*9*, *20*). The apparent decrease of the η/s ratio as the energy approaches the ground state $0.48E_F$ (*9*) does not require that the local ratio $\rightarrow 0$ as $T \rightarrow 0$ because contributions from the cloud edges significantly increase S as compared with the local s at the center.

References and Notes

1. K. M. O'Hara, S. L. Hemmer, M. E. Gehm, S. R. Granade, J. E. Thomas, *Science* **298**, 2179 (2002).
2. S. Giorgini, L. P. Pitaevskii, S. Stringari, *Rev. Mod. Phys.* **80**, 1215 (2008).
3. I. Bloch, J. Dalibard, W. Zwerger, *Rev. Mod. Phys.* **80**, 885 (2008).
4. W. Ketterle, M. W. Zwierlein, "Making, probing and understanding ultracold Fermi gases," in *Ultracold Fermi Gases, Proceedings of the International School of Physics "Enrico Fermi,"* Course CLXIV, Varenna, 20 to 30 June 2006 (IOS Press, Amsterdam, 2008).
5. J. Kinast *et al.*, *Science* **307**, 1296 (2005).
6. L. Luo, B. Clancy, J. Joseph, J. Kinast, J. E. Thomas, *Phys. Rev. Lett.* **98**, 080402 (2007).
7. J. T. Stewart, J. P. Gaebler, C. A. Regal, D. S. Jin, *Phys. Rev. Lett.* (2006).
8. H. Hu, P. D. Drummond, X.-J. Liu, *Nat. Phys.* **3**, 469 (2007).
9. L. Luo, J. E. Thomas, *J. Low Temp. Phys.* **154**, 1 (2009).
10. M. Horikoshi, S. Nakajima, M. Ueda, T. Mukaiyama, *Science* **327**, 442 (2010).
11. S. Nascimbène, N. Navon, K. J. Jiang, F. Chevy, C. Salomon, *Nature* **463**, 1057 (2010).
12. P. K. Kovtun, D. T. Son, A. O. Starinets, *Phys. Rev. Lett.* **94**, 111601 (2005).
13. L. P. Csernai, J. I. Kapusta, L. D. McLerran, *Phys. Rev. Lett.* **97**, 152303 (2006).
14. B. A. Gelman, E. V. Shuryak, I. Zahed, *Phys. Rev. A* **72**, 043601 (2005).
15. G. M. Bruun, H. Smith, *Phys. Rev. A* **75**, 043612 (2007).
16. T. Schäfer, *Phys. Rev. A* **76**, 063618 (2007).
17. A. Turlapov *et al.*, *J. Low Temp. Phys.* **150**, 567 (2008).
18. The experiments were performed far from p-wave Feshbach resonances. The relevant threshold energy for p-wave scattering was then comparable with the barrier height. Using the known C_6 coefficients, the barrier height for ^{40}K is 280 μK, whereas for ^{6}Li the barrier height is 8 mK. Hence, for temperatures in the μK range as used in the experiments, p-wave scattering is negligible, and s-wave scattering dominates.
19. J. Kinast, A. Turlapov, J. E. Thomas, *Phys. Rev. Lett.* **94**, 170404 (2005).
20. Materials and methods are available as supporting material on *Science* Online.
21. D. T. Son, *Phys. Rev. Lett.* **98**, 020604 (2007).
22. M. A. Escobedo, M. Mannarelli, C. Manuel, *Phys Rev. A*, http://arxiv.org/abs/0904.3023v2.
23. T.-L. Ho, *Phys. Rev. Lett.* **92**, 090402 (2004).
24. J. E. Thomas, J. Kinast, A. Turlapov, *Phys. Rev. Lett.* **95**, 120402 (2005).
25. T. Schäfer, http://arxiv.org/abs/1008.3876v1.
26. C. Menotti, P. Pedri, S. Stringari, *Phys. Rev. Lett.* **89**, 250402 (2002).
27. P. Massignan, G. M. Bruun, H. Smith, *Phys. Rev. A* **71**, 033607 (2005).
28. We give the damping rate $1/\tau$ for a cylindrically symmetric cigar-shaped trap. For $\delta \equiv (\omega_x - \omega_y)/\sqrt{\omega_x\omega_y} << 1$, with ω_x,ω_y the transverse trap frequencies, $1/\tau$ contains an additional factor $1 - \delta$.
29. H. Guo, D. Wulin, C.-C. Chien, K. Levin, http://arxiv.org/abs/1008.0423v3.
30. E. Taylor, M. Randeria, *Phys. Rev. A* **81**, 053610 (2010).
31. T. Enss, R. Haussmann, W. Zwerger, http://dx.doi.org/10.1016/j.aop.2010.10.002.
32. T. Scäfer, C. Chafin, http://arxiv.org/abs/0912.4236v3.

33. This research is supported by the Physics Divisions of NSF, the Army Research Office, the Air Force Office Office of Sponsored Research, and the Division of Materials Science and Engineering, the Office of Basic Energy Sciences, Office of Science, U.S. Department of Energy. J.E.T. and T.S. thank the ExtreMe Matter Institute (EMMI) for hospitality.

Supporting Online Material

www.sciencemag.org/cgi/content/full/science.1195219/DC1
Materials and Methods
Figs. S1 and S2
References

16 July 2010; accepted 24 November 2010
Published online 9 December 2010;
10.1126/science.1195219

Time-Resolved Holography with Photoelectrons

Y. Huismans,[1]* A. Rouzée,[1,2] A. Gijsbertsen,[1] J. H. Jungmann,[1] A. S. Smolkowska,[1] P. S. W. M. Logman,[1] F. Lépine,[3] C. Cauchy,[3] S. Zamith,[4] T. Marchenko,[5] J. M. Bakker,[6] G. Berden,[6] B. Redlich,[6] A. F. G. van der Meer,[6] H. G. Muller,[1] W. Vermin,[7] K. J. Schafer,[8] M. Spanner,[9] M. Yu. Ivanov,[10] O. Smirnova,[2] D. Bauer,[11] S. V. Popruzhenko,[12] M. J. J. Vrakking[1,2]*

Ionization is the dominant response of atoms and molecules to intense laser fields and is at the basis of several important techniques, such as the generation of attosecond pulses that allow the measurement of electron motion in real time. We present experiments in which metastable xenon atoms were ionized with intense 7-micrometer laser pulses from a free-electron laser. Holographic structures were observed that record underlying electron dynamics on a sublaser-cycle time scale, enabling photoelectron spectroscopy with a time resolution of almost two orders of magnitude higher than the duration of the ionizing pulse.

After a strong laser field ionizes an atom or molecule, the liberated electron is accelerated by the oscillatory laser electric field and driven back toward the ion (*1*). Electron-ion recollision leads to the emission of extreme ultraviolet (XUV) radiation, with a duration that approaches the atomic unit of time (24.2 as) (*2*, *3*) and encodes detailed structural and dynamical information about the atomic or molecular medium used (*4*–*7*). Alternatively, the returning electron may elastically or inelastically scatter (*8*, *9*). These processes benefit from the 10^{11} A/cm^2 electron recollision current incident on the target ion, exceeding current densities used in transmission electron microscopes (*10*). The laser-driven electron motion is fully coherent, allowing one to put into practice the concept of holography (*11*) and to extend it to electron-ion collisions involving laser-ionized and -driven photoelectrons (*9*, *12*, *13*). We show how under suitably chosen experimental conditions, a hologram can be recorded that encodes temporal and spatial information both about the ion (the "target") and the recollision electron (the "source"), opening the way to a new type of ultrafast photoelectron spectroscopy of electron and nuclear dynamics in molecules.

Key to holographic electron imaging is the observation of an interference pattern between a reference wave, which is emitted from the source and does not interact with the target, and a signal wave, which scatters off the target and encodes its structure. The encoded information is stored when the signal wave interferes with the reference wave on a detector. A simple analysis borrowed from ray optics (Fig. 1A) shows that because of path length differences, a phase difference $\Delta\varphi = (k - k_z)z_0$ (where k is the total momentum, k_z is the momentum in the z direction, and z_0 is the distance to the scattering center) arises between the reference and scattered waves, resulting in the pattern shown in Fig. 1B.

To record a clear holographic picture, it is desirable that the reference wave not be influenced by the positively charged target and, therefore, that the electron source is located at some distance from the target, z_0. A suitable way to

---

[1] FOM Institute AMOLF, Science Park 113, 1098 XG Amsterdam, Netherlands. [2] Max-Born-Institut, Max Born Straße 2A, D-12489 Berlin, Germany. [3] Université Lyon I, CNRS, Laboratoire de Spectrométrie Ionique et Moléculaire, UMR 5579, Bâtiment. Kastler, 43, Boulevard du 11 Novembre 1918, F69622 Villeurbanne Cedex, France. [4] Laboratoire Collisions, Agrégats, Réactivité, Institut de Recherche sur les Systèmes Atomiques et Moléculaires Complexes, UPS, Université de Toulouse and UMR 5589 CNRS, 31062 Toulouse, France. [5] Université Pierre et Marie Curie Université Paris 6, CNRS, UMR 7614, Laboratoire de Chimie Physique-Matière et Rayonnement, 11 rue Pierre et Marie Curie, F-75005 Paris, France. [6] FOM-Institute for Plasma Physics Rijnhuizen, Edisonbaan 14, 3439 MN Nieuwegein, Netherlands. [7] SARA Computing and Networking Services, Science Park 121, 1098 XG Amsterdam, Netherlands. [8] Department of Physics and Astronomy, Louisiana State University (LSU), Baton Rouge, Louisiana 70803–4001, USA. [9] National Research Council of Canada, Ottawa, Ontario K1A 0R6, Canada. [10] Department of Physics, Imperial College, London SW7 2BW, UK. [11] Institut für Physik, Universität Rostock, 18051 Rostock, Germany. [12] Moscow Engineering Physics Institute, National Research Nuclear University, Kashirskoe Shosse 31, Moscow, 115409, Russia.

*To whom correspondence should be addressed. E-mail: huismans@amolf.nl (Y.H.); marc.vrakking@mbi.berlin.de (M.J.J.V.)